Supplementary Materials For

Engineering robust oxygen vacancy towards efficient toluene purification: Coupling crystal facet with Mn-Ce solid solution

Xi Chen[a,b], Yanyan Zhang[a,b], Wei Dai[a,b], Jiaxin Geng[a,b], Xinxin Wang[b,c], Haiyang Li[a,b], Shouxin Xin[a,b], Zhongxian Song[d], Wei Liu[b,c,*],Xuejun Zhang[a,b,*]

[a]College of Environmental and Safety Engineering, Shenyang University of Chemical Technology, Shenyang 110142, China

[b]Shenyang Key Laboratory of Chemical Pollution Control, Shenyang University of Chemical Technology, Shenyang 110142, China.

[c]College of Science, Shenyang University of Chemical Technology, Shenyang, China

[d]Faculty of Environmental and Municipal Engineering, Henan University of Urban Construction, Pingdingshan 467036, China

*Corresponding authors.

E-mail addresses: xjzhang_syict@163.com

Table of contents:

1. Detailed information for catalyst characterization

XRD spectra of the catalysts were obtained using a Bruker D8 Advance powder X-ray diffractometer equipped with a Cu Kα radiation source to determine relevant parameters including crystal phase and grain size. A complete diffraction pattern was obtained by using a fixed step size of 0.02° with a dwell time of 2 s per step over a 2θ angle ranging from 10° to 80°. Subsequently, the resulting data were processed according to Scherrer's formula in order to calculate the dimensions of the microcrystals:

$$d = \frac{k \cdot \lambda}{\beta \cdot cos\theta} \quad (1)$$

where d is the average size of the ordered (crystalline) domains, which may be smaller or equal to the grain size, k (0.9) is the shape factor, λ (0.154184 nm) is the X-ray wavelength, β is the line broadening at half the maximum intensity (FWHM) in radians, and θ is the Bragg angle.

The FWHM (full width at half maximum) was calculated from the line broadening of the six most intense XRD reflections of CeO_2 (111) crystal planes. Lattice constant (a) was computed from the following equation based on the (111) crystal planes ofCeO_2:

$$a = \frac{\lambda}{2sin\theta}\sqrt{h^2 + k^2 + l^2} \quad (2)$$

where h, k, l are Miller indices of CeO_2.

Raman measurements of the samples were performed in VIA Microscope Raman using a RENISHAW with a 532 nm solid-state laser as the excitation source. The testing range was from 100 to 900 cm^{-1}.

Samples (10 mg) were subjected to EPR testing on a Bruker A300-10 under ambient conditions without light illumination.

Sample calculations for Brunauer-Emmett-Teller (BET) surface area and total pore volume are based on N_2 adsorption-desorption isotherms, which are obtained automatically by Tristar II 3020 at liquid N_2 temperature (-196 ^oC).

The scanning electron microscopy (SEM, HITACHI SU8010), the transmission electron microscopic (TEM) and high-resolution transmission electron microscopic (HRTEM, FEI F20) were applied to observe the morphology and space structural details of catalysts.

H_2-TPR was conducted using a chemisorption instrument (PCA-1200). Typically, 20 mg of the catalyst was placed in a u-type quartz tube and pre-treated in a pure N_2 stream. The temperature

was increased to 400 °C at the rate of 20 °C/min and maintained for 40 min; then, it was decreased to 100 °C. The following samples were reduced via an Ar gas mixture with 8% H_2, and the total flow rate was 30 mL/min. The H_2 consumption was measured by a thermal conductivity detector (TCD), during the temperature was gradually increased to 900 °C.

O_2-TPD was carried out by the chemisorption instrument (BETCAT-A). The 100 mg sample was placed in a u-shaped quartz tube, and then subjected to pretreatment for 60 min at 200 °C in a pure He gas stream at 30 mL/min, oxygen uptake for 60 min at 50 °C in a 20 vol.% O_2 gas stream at 30 mL/min, sweeping for 10 min at 50 °C in a He gas stream, a warming and desorption process which is heated at 10 °C/min to 900 °C in a pure He atmosphere and detection by TCD.

Electrochemical impedance spectroscopy (EIS) was performed with the electrochemical workstation (GAMRY Reference 3000) in Na_2SO_4 electrolytes by employing Ag/AgCl electrode an Pt wire as the reference electrode and counter electrode, respectively.

The light absorption spectra of samples were collected by ultraviolet–visible diffuse reflectance spectra (UV-vis DRS, Shi-madzu UV 2600, Japan), with $BaSO_4$ powder as the reference.

Electrochemical measurements (Tafel curve) were performed in a standard three-electrode cell with a Pt plate electrode (Pt, 99.99 %) as the counter electrode and a saturated calomel electrode (SCE, 3M KCl, 207mV vs. SCE at 25 °C) as the reference electrode. A Luggin capillary was used with its tip positioned at 1-2mm from the surface ofworking electrode in order to minimize errors caused by IR drop in the electrolyte. The measurements were carried out with an electrochemical workstation (CHI 660E) controlled by a PC. 0.5 mol/L Na_2SO_4 was chosen as the electrolyte solution and scanned at a rate of 5 mV/s in the range of 0 ~ 1.5 V vs. SCE to obtain the Tafel curve of the electrode.

Toluene temperature-programmed desorption (Toluene-TPD, PCA-1200): the samples were pre-treated under Ar gas atmosphere at 10 °C/min to 150 °C, then cooled down to 50 °C. After that, the catalyst was purged with He (99.999 %) gas carrying toluene gas for 30 minutes to saturation, and then switched to pure He gas to sweep the physically adsorbed toluene away from the catalyst surface. Subsequently, the helium carrier gas was introduced into the sample at 50 °C with a flow rate of 30 mL/min and the TCD detector was turned on to stabilize the signal line. After the signal line was stable, the temperature was increased to 800 °C at the rate of 10 °C/min for temperature rise and desorption. Toluene, CO_2 and O_2 were monitored with an MS-200 multi-component gas

analyzer during the TPD process described above, with m/z ratios of 44 and 32, respectively.

XPS spectra were acquired by the Escalab 250Xi photoelectron spectrometer. The binding energy (BE) scales of Ce, Mn, and O were corrected for charging the samples using the C1s peak of adventitious carbon at 284.8 eV as a reference.

In situ diffused reflectance infrared Fourier transform spectra (in-situ DRIFTS) was recorded of the toluene oxidation on a Nicolet IS 10 FT-IR spectrometer, equipped with a MCT detector. Prior to recording the background scan, the catalyst was pretreated at 300 ^{o}C for 30 min under a 20 vol.% O_2 flow (100 mL/min). Then, the O_2 flow was switched to the toluene gas flow for 30 min before the sample spectrum was recorded at the same temperature as the background scan. Then the spectra were recorded at different target temperatures and times.

2. Evaluation of catalytic activity

The testing of catalyst properties was implemented in a fixed bed micro-reactor. The first step was to prepare the catalyst using a tablet press and sieve the sample through a 40-60 mesh sieve. Next, 100 mg of catalyst was poured into a T-shaped quartz tube with an inner diameter of 8 mm and an outer diameter of 10 mm, and the ends of the tube were filled with quartz cotton to prevent the catalyst powder from entering the chromatography system, thus avoiding clogging of the tube. The setup conditions for the catalytic reaction included a gas mixture of toluene and dry air at a flow rate of 100 mL min^{-1}, a gas composition of 20 vol.% O_2/N_2, a toluene concentration of 500 ppm, nitrogen as the equilibrium gas, and an airspeed set to 6000 h^{-1}. The exhaust gas from the reaction was introduced into a Fuli 9790 type GC and detected on-line using a flame ionization detector (FID) to analyze the concentration of the emitted gases. The performance of the catalyst was evaluated in the range of 100 to 340 °C. The conversion of toluene (X %), the reaction rate (r, mol^{-1} s^{-1}), and the carbon dioxide selectivity (X_{CO2} %) were calculated as follows:

$$X_{toluene} = \frac{C_{in} - C_{out}}{C_{in}} \times 100\ \% \tag{3}$$

$$r = \frac{\mathrm{F} \times X_{toluene}}{\mathrm{w} \times S_{BET}} \tag{4}$$

$$X_{CO_2} = \frac{C}{\mathrm{C_{CO_2}}} \times 100\ \% \tag{5}$$

Cin represents the initial concentration of toluene and Cout represents the concentration of toluene after the reaction. F is the gas molecular flow rate (mol/s), W is the mass of the catalyst (g), and SBET refers to the specific surface area of the catalyst (m^2/g). XCO_2 denotes the theoretical concentration of carbon dioxide produced when toluene is completely oxidized, while C denotes the concentration of carbon dioxide that is actually measured at different temperatures.

3. Figures and tables

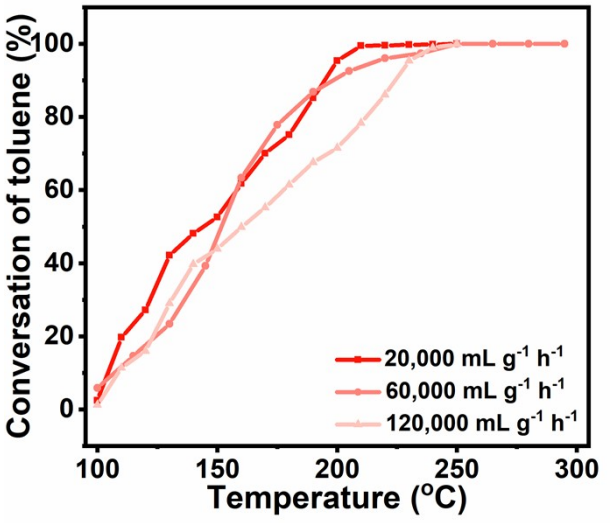

Fig. S1. The effect of GHSV on the toluene conversion over 3Ce1Mn catalyst.

As shown in Fig. S1, the activity of the 3Ce1Mn catalyst remained stable at GHSV below 60,000 mL g^{-1} h^{-1} and was not affected by changes in airspeed. However, the activity decreased slightly when the airspeed was increased to 120,000 mL g^{-1} h^{-1} (T_{90} = 221 °C). Notably, 3Ce1Mn showed good airspeed adaptability at 60,000 mL g^{-1} h^{-1} GHSV, suggesting that it can effectively enhance the toluene removal efficiency at constant temperature, which is potentially promising for industrial applications.

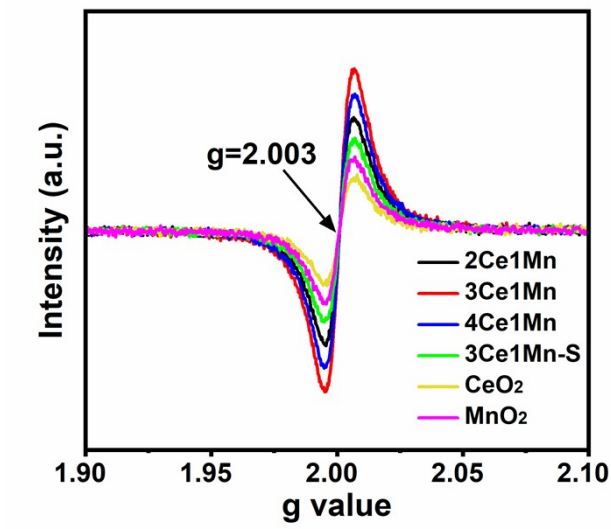

Fig. S2. EPR of the prepared catalysts.

Fig. S2 shows the EPR spectra of a number of samples where the peak intensities are correlated with the O_v concentration. It can be inferred that the magnitude of the O_v content is in the order of 3Ce1Mn > 4Ce1Mn > 2Ce1Mn > MnO_2 > CeO_2. This result further confirms that the formation of

the solid solution structure and the exposure of a particular crystalline surface generates a large number of oxygen defects and reactive oxygen species, in agreement with the previous characterization results.

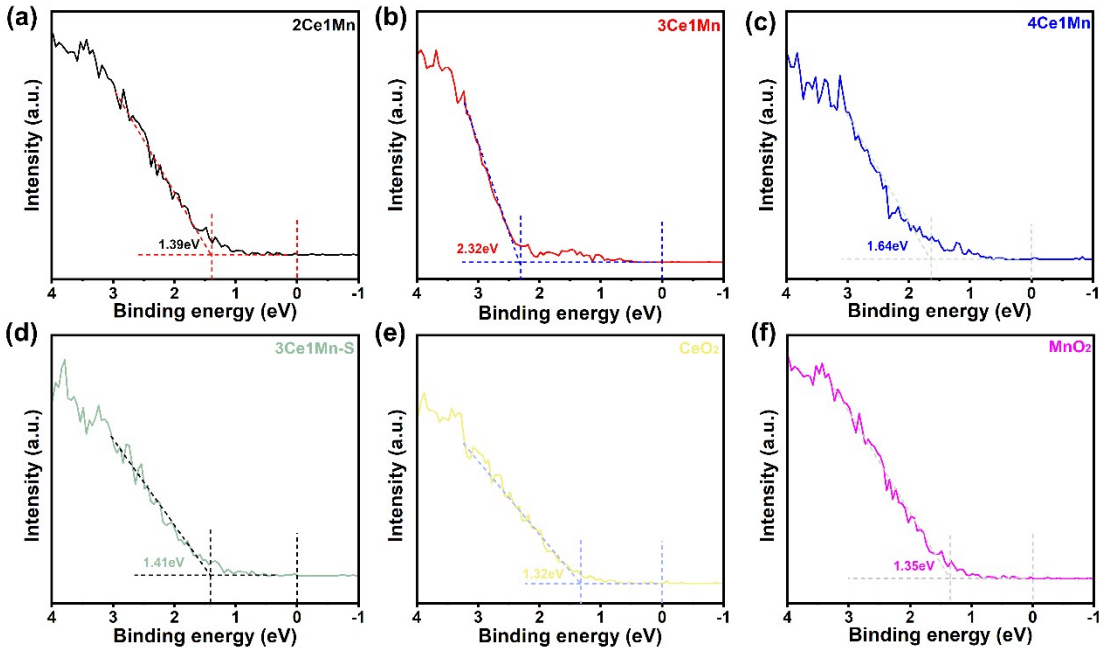

Fig. S3. XPS valence spectra of the prepared catalysts.

The ordering of the valence band positions of each sample is shown in Fig. S3, where 3Ce1Mn is the highest with 2.32 eV, followed by 4Ce1Mn (1.64 eV), 3Ce1Mn-S (1.41 eV), 2Ce1Mn (1.39 eV), MnO_2 (1.35 eV) and CeO_2 (1.32 eV). 3Ce1Mn has the highest valence band value, indicating that it has the most pronounced adsorption capacity for reactants.

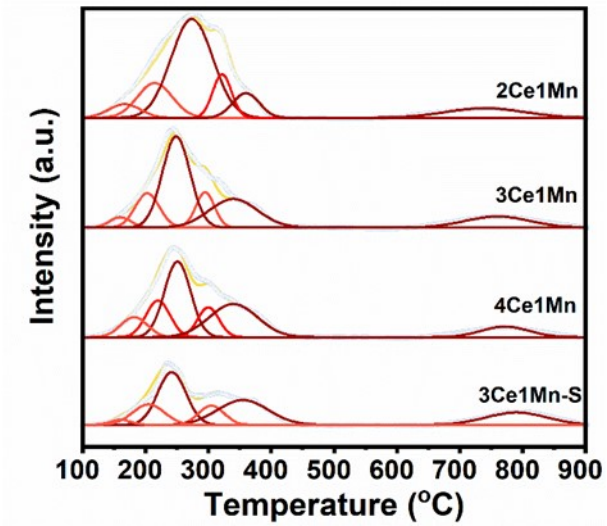

Fig. S4. H_2-TPR plot of the prepared catalysts.

According to the results of XPS analysis, elemental Ce exists in the catalyst in a mixed valence

state of Ce^{3+} and Ce^{4+}, while elemental Mn coexists in a multivalent state of Mn^{4+}, Mn^{3+} and Mn^{2+} multivalent states coexist, indicating the existence of dynamic redox processes in the system. Based on this valence distribution feature and the reduction process of the species, the H_2-TPR spectra (Fig. S4) were deconvolutionally analyzed by split-peak processing, and the reduction peaks were classified into five phases according to the ascending order of temperatures, which were $MnO_2 \rightarrow Mn_2O_3$, $Mn_2O_3 \rightarrow Mn_3O_4$, $Ce^{4+} \rightarrow Ce^{3+}$ at surface, $Mn_3O_4 \rightarrow MnO$, $Ce^{4+} \rightarrow Ce^{3+}$ in bulk, with the high-temperature region above 600 °C corresponding to the reduction process of the CeO_2 bulk phase structure [1]. It is noteworthy that the hydrogen consumption ratios of Mn and Ce obtained by peak splitting integrals are in better agreement with the results of the ICP elemental quantitative analysis, which provides an important support for the rationality of the peak splitting strategy. The average oxidation state (AOS) of Mn in $CeMnO_x$ catalysts was calculated based on the reduction peak of Mn according to the peak splitting results of H_2-TPR. It can be found that the average oxidation states (AOS) of Mn for 2Ce1Mn, 3Ce1Mn, 4Ce1Mn and 3Ce1Mn-S series catalysts are 3.17, 3.12, 3.22 and 3.3, respectively. Combined with the results of Mn3s in XPS, it can be found that the lowest average oxidation state of 3Ce1Mn may be due to the presence of Ce^{4+} and Ce^{3+} in the catalyst together reducing a large number of Mn^{4+} species.

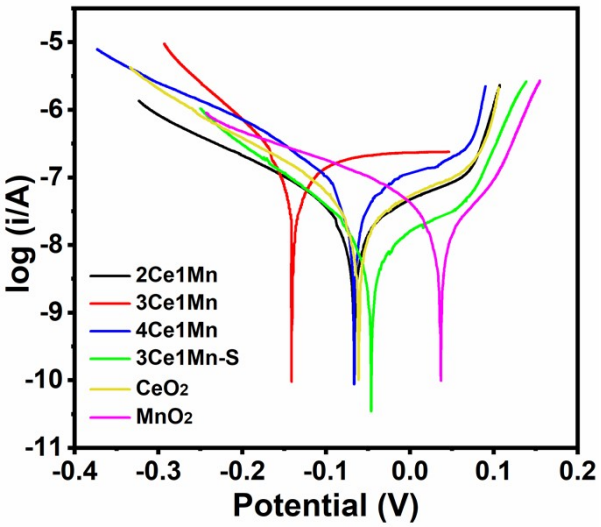

Fig. S5. Tafel plot of the prepared catalysts.

The Tafel polarization curves are shown in Fig. S5, which are able to verify the electron transfer ability of the catalysts. The corrosion potential is an indicator of a catalyst's capacity to release electrons. Since the lowest corrosion potential is observed in 3Ce1Mn, which signifies a high electron transfer efficiency and, consequently, augmented catalyst activity.

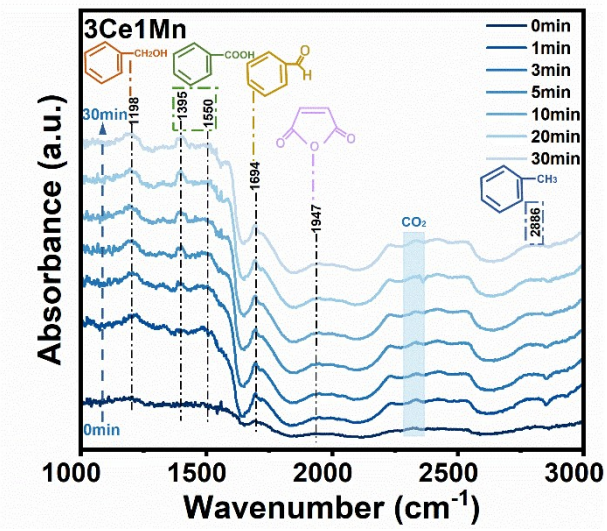

Fig. S6. In-situ DRIFTS of 3Ce1Mn catalyst exposure to toluene in air for different time.

The time-dependent in situ DRIFTS of 3Ce1Mn are shown in Fig. S6, where benzyl alcohol (1198 cm^{-1}), benzaldehyde (1694 cm^{-1}), benzoic acid (1395, 1550 cm^{-1}) and maleic anhydride (1947 cm^{-1}) appeared successively as the reaction progressed up to one minute and reached the maximum value with increasing time. Therefore, the combination of temperature and time in situ DRIFTS suggested the following oxidation pathway for toluene over 3Ce1Mn catalyst: toluene → benzyl alcohol → benzaldehyde → benzoic acid → maleic anhydride → H_2O and CO_2.

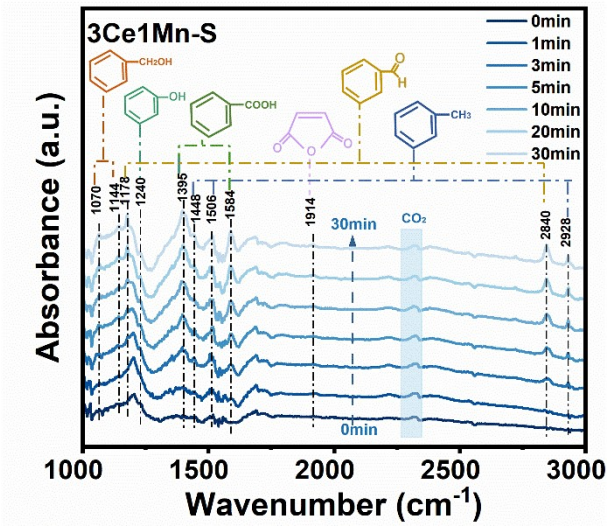

Fig. S7. In-situ DRIFTS of 3Ce1Mn-S catalyst exposure to toluene in air for different time.

Fig. S7 illustrates the in situ DRIFTS of 3Ce1Mn-S over time, capturing a range of intermediates including benzyl alcohol, benzaldehyde, benzoic acid, phenol, and maleic anhydride

in agreement with the temperature change. A sustained accumulation of benzoic acid was observed, implying that the oxidation of benzoic acid is a key step in the overall reaction process. In particular, a characteristic peak of phenol species was detected on 3Ce1Mn-S (1240 cm^{-1}), which shows a different reaction pathway compared to 3Ce1Mn. This finding reveals that the oxidation of toluene on 3Ce1Mn-S is more complex, and the oxidation pathway involves a series of reactions starting from toluene and sequentially passing through benzyl alcohol, benzaldehyde, benzoic acid, phenol, maleic anhydride, and ultimately converted to CO_2 and H_2O.

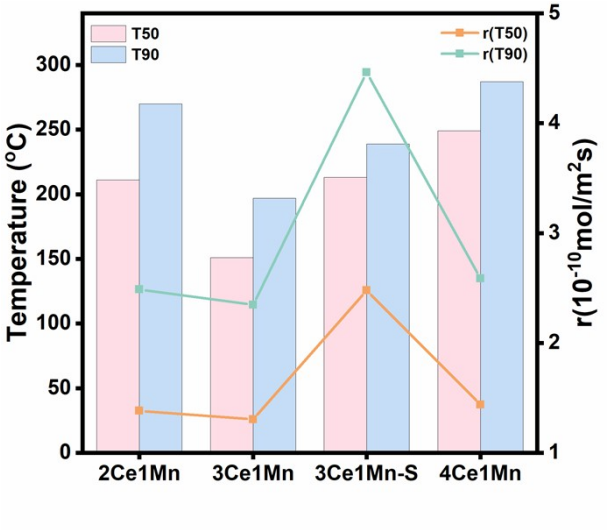

Fig. S8. Toluene conversion after normalization of specific surface area for the prepared catalysts.

In order to further elucidate whether the specific surface area of the catalysts is a key factor affecting their catalytic performance, the toluene conversion of each catalyst was calculated after normalization by specific surface area, as shown in Fig. S8. It can be observed that the 3Ce1Mn exhibits a relatively low conversion efficiency of toluene per unit area of active sites. However, due to its substantial specific surface area and numerous active sites, it ultimately demonstrates the most favourable performance per unit mass. The results indicate that the specific surface area of the catalyst has a great influence on the activity of the catalyst.

Table S1. Catalytic performance of CeMn catalysts for the oxidation of toluene as reported in the recent literature.

Catalyst	Toluene (ppm)	WHSV (mL g^{-1} h^{-1})	T_{90} (°C)	Ref.
Mn(C)Ce(C)SOL	1000	30 000	235	[2]
$CeMnO_3$-0.2	1000	30 000	247	[3]
MnCe-OH	1000	36 000	236	[4]
CeMn-0.4	1000	48 000	242	[5]
3Mn2Ce	1000	30 000	236	[6]
CM-HT	1000	60 000	246	[7]
CeO_2-MnO_x	500	60 000	261	[8]
10%CeO_2-MnO_x	1000	48 000	265	[9]
CM-R	500	40 000	256	[10]
CeMn-140 °C	500	60 000	255	[11]
2Ce1Mn	500	60000	270	This work
3Ce1Mn	500	60 000	195	This work
4Ce1Mn	500	60 000	239	This work
3Ce1Mn-S	500	60 000	287	This work

Table S2. ICP results of the prepared catalysts.

Sample	Ce (wt%)	Mn (wt%)	K (wt%)	O (wt%)	Ce/Mn (mol)
2Ce1Mn	68.57	11.48	0.01	19.94	2.3
3Ce1Mn	71.65	9.52	0.19	18.64	2.9
4Ce1Mn	74.31	7.44	0.24	18.01	3.9
3Ce1Mn-S	72.23	9.94	0.13	17.70	2.8
MnO_2	0	55.10	15.44	29.46	/
CeO_2	82.45	0	0	17.55	/

4. References

[1] X. Li, R. Chen, M. Yang, Y. Niu, J. Li, D. Shao, X. Zheng, C. Zhang, Y. Qi, Insight into modified CeMn based catalysts for efficient degradation of toluene by in situ infrared, Science of The Total Environment 912 (2024) 169192.

[2] Z. Chen, J. Zhou, X. Zhuge, Z. Xie, K. Du, Catalytic oxidation of toluene over highly dispersed Mn-Ce solid solutions synthesized with weakly acidic precursors, Process Safety and Environmental Protection 179 (2023) 208-227.

[3] J. Wang, J. Su, G. Zhao, D. Liu, H. Yuan, A.T. Kuvarega, B.B. Mamba, H. Li, J. Gui, A facile method for preparing the $CeMnO_3$ catalyst with high activity and stability of toluene oxidation: The critical role of small crystal size and Mn^{3+}-Ov-Ce^{4+} sites, Journal of Hazardous Materials 470 (2024) 134114.

[4] L. Li, C. Zhang, J. Yan, D. Wang, Y. Peng, J. Li, J. Crittenden, Distinctive Bimetallic Oxides for Enhanced Catalytic Toluene Combustion: Insights into the Tunable Fabrication of Mn−Ce Hollow Structure, ChemCatChem 12(10) (2020) 2872-2879.

[5] Y. Jiang, Y. Jiang, Y. Xu, X. Sun, S. Cheng, Y. Liu, X. Dou, Z. Yang, Ce-based three-dimensional mesoporous microspheres with Mn homogeneous incorporation for toluene oxidation, Journal of Colloid and Interface Science 670 (2024) 785-797.

[6] X. Zhang, F. Bi, Z. Zhu, Y. Yang, S. Zhao, J. Chen, X. Lv, Y. Wang, J. Xu, N. Liu, The promoting effect of H_2O on rod-like $MnCeO_x$ derived from MOFs for toluene oxidation: A combined experimental and theoretical investigation, Applied Catalysis B: Environmental 297 (2021) 120393.

[7] X. Zhang, J. Zhao, Z. Song, W. Liu, H. Zhao, M. Zhao, Y. Xing, Z.a. Ma, H. Du, The catalytic oxidation performance of toluene over the Ce-Mn-O_x catalysts: Effect of synthetic routes, Journal of Colloid and Interface Science 562 (2020) 170-181.

[8] K. Zhang, Y. Ge, J. Zhu, N. Li, H. Luo, B. Li, Z. Zhao, W. Wu, Surface characteristics and catalytic activity of modified rare earth concentrate for low-temperature selective catalytic reduction of NO_x with NH_3, Materials Chemistry and Physics 242 (2020) 122421.

[9] K. Zhang, J. Wang, P. Guan, N. Li, Z. Gong, R. Zhao, H. Luo, W. Wu, Low-temperature NH_3-SCR catalytic characteristic of Ce-Fe solid solutions based on rare earth concentrate, Materials Research Bulletin 128 (2020) 110871.

[10] Y. Wang, W. Deng, Y. Wang, L. Guo, T. Ishihara, A comparative study of the catalytic oxidation of chlorobenzene and toluene over Ce-Mn oxides, Molecular Catalysis 459 (2018) 61-70.

[11] Z. Huang, J. Zhao, Z. Song, W. Liu, X. Zhang, Y. Mao, H. Zhao, M. Zhao, S. Liu, Z. Wang, Controllable construction of Ce-Mn-O with tunable oxygen vacancies and active species for toluene catalytic combustion, Applied Organometallic Chemistry 34(12) (2020) e5958.